Aerospace Science and Technology 175 (2026) 111978

Contents lists available at ScienceDirect

Aerospace Science and Technology

journal homepage: www.elsevier.com/locate/aescte

Multi-point surrogate-based aerodynamic optimisation of a generic hypersonic waverider

Jade Nassif [a,1], Jimmy-John OE Hoste [b], Tamás István Józsa [a,*]

[a] Centre for Assured and Connected Autonomy, Cranfield University, College Road, Cranfield, MK43 0AL, UK
[b] Destinus SA, Aeropole 132, Payerne, 1530, Switzerland

ARTICLE INFO

Communicated by Dr Mehdi Ghoreyshi

Keywords:
Waverider
Inviscid CFD
Aerodynamic shape optimisation
Hypersonic flight
Osculating cone
Genetic algorithm
Kriging surrogate model

ABSTRACT

For atmospheric flight at hypersonic speeds, waverider designs offer the benefit of higher aerodynamic performance by sustaining an attached shock wave at the leading edge. Inverse design methods are typically used to generate waverider shapes by combining an *a priori* desired flow field with streamline-tracing starting from the rear of the vehicle. A difficulty of these inverse design methods is to perform valid parameter space explorations or design optimisation tasks, for which direct optimisation frameworks are better suited. This work builds on the direct optimisation approach introduced by Son *et al.* (Aerospace, Vol 9, Issue 7, 2022, 348) in which four parameters are used to define waverider shapes. An in-depth exploration of the design space is presented based on similar methods consisting of inviscid CFD-derived surrogate modelling followed by genetic algorithm-based optimisation of aerodynamic performance and internal volume. Focus is placed on software accessibility and the wide-speed problem approached through a cost function incorporating information from simulations at multiple Mach numbers. The established open-source framework enables systematic and computationally tractable exploration of waverider design spaces, establishing a reproducible and extensible optimisation infrastructure for hypersonic configuration development.

1. Introduction

Several vehicles relying either fully or partially on waveriding have been experimentally studied and flight tested over the past two decades including the X-43 [1] (winged-body/waverider configuration), the X-51 [2] (forebody waverider), the HTV-2 [3] (lifting body with high lift over drag characteristics of waveriders [4]), various HIFiRE [5] configurations, HEXAFLY-INT [6] and the GHGV-2 [7]. These geometries are typically constructed for a specific flow field (a design Mach number and shock wave shape) [8], analytically or through streamline-tracing methods. The nature of the basic flow fields can be two-dimensional [9–15] ("wedge-derived", "caret" or "Λ" waveriders), axi-symmetric (cone-derived) [10,11,16,17], three-dimensional [10,11,18–25] or combinations of the previous main types [10,11,26–28]. Waveriders can be generated with either a direct method (parametrised geometry, e.g. [26,27,29–31]) or through inverse methods (streamline-tracing). It is worth noting that some of the direct methods still require streamline-tracing as part of the geometry generation process. As pointed out by Lewis [32], any vehicle shape with a presented leading edge angle below the shock wave attachment limit can be considered a waverider. In general, the inverse approaches have gained popularity, especially since the introduction of the osculating cone method by Sobieczky *et al.* [23]. Regardless of the specific inverse design of choice, the method remains unchanged as detailed in Ding et al. [11], Zhao et al. [28], Son et al. [31].

Inverse-design methods are unable to assess *a priori* the desired aerodynamic performance as well as obtain geometrical information such as internal volume [31]. These limitations undermine shape optimisation. Once the geometry is generated, the geometrical information can be assessed and the aero-thermodynamic performance can be obtained via impact methods [33,34]. However, the general use of Computational Fluid Dynamics (CFD) has become more affordable and widespread. Inviscid simulations are particularly popular and these can be augmented through viscous corrections [7,35–39] instead of solving the more costly turbulent problem via the Reynolds-Averaged Navier-Stokes (RANS) equations. A general disadvantage of the resulting waverider designs is the problem of reduced performance at off-design conditions. The so called wide-speed operating problem of waveriders has been addressed in several previous investigations [28,40–45]. The current study revisits this issue in the context of waverider shape optimisation based on cost function engineering. Whereas aerodynamic stability and heating

* Corresponding author.
E-mail addresses: jimmyjohn.hoste@destinus.ch (J.-J.O. Hoste), tamas.jozsa@cranfield.ac.uk (T.I. Józsa).
[1] Currently at Haas F1 Team, Banbury, UK

https://doi.org/10.1016/j.ast.2026.111978
Received 13 December 2025; Received in revised form 11 February 2026; Accepted 19 February 2026
Available online 20 February 2026
1270-9638/© 2026 The Authors. Published by Elsevier Masson SAS. This is an open access article under the CC BY license (http://creativecommons.org/licenses/by/4.0/).

are other challenging topics in waverider shape design, these aspects will not be considered in this study. For further details about the aerodynamic stability and heating of waveriders, the reader is referred to [46–51] and [31,52–66], respectively.

To design a waverider, optimisation algorithms are conventionally used together with single- or multi-objective functions that consider one or more of the previously discussed design criteria (e.g. volume, aerodynamic performance, heating and stability). Previously, gradient-based algorithms have been tested [67]. However, there is a risk of getting stuck in a local optimum and the computational cost linked to computing the gradients increases with the number of design variables. The issue of gradient computation expenses can be overcome through adjoint-based methods which solve a set of differential equations to obtain all gradients at once [68]. Adjoint-based optimisation combined with CFD is gaining popularity in aerodynamic shape optimisation because this approach can handle a large number of design variables (e.g., all points of the surface mesh) and therefore allows for direct control of the shape through its mesh surface points. However, it has been demonstrated [37,38,69,70] that adjoint-based optimisation methods get easily stuck in a local optimum. A potentially different approach within adjoint-based CFD is the use of free-form deformation through a reduced set of control points instead of considering the complete surface mesh of the vehicle of interest as exemplified by Qu *et al.* [71]. A multi-disciplinary optimisation (MDO) approach was also taken by Morita *et al.* [72] using an adjoint-based optimiser, accounting for trajectory-aero-structural coupling.

Gradient-free optimisation algorithms aim to find the global optimum by direct search of the design space. An efficient parametrisation with good design space coverage can reduce their general cost and make search algorithms more practical for aerodynamic shape optimisation [67,73] - at the expense of potentially missing the exact global optimum. Within the waverider literature, search-based algorithms have been considered in the past [29,63,74,75]. Of particular interest is the MDO of air breathing waveriders by Bowcutt [33], where the objective to maximise mission range while accounting for multi-disciplinary variables resulted in a 46 % increase from the baseline. However, waverider optimisation through a well-defined direct design framework, derived from inverse-design method has not commonly been adopted. The work by Son *et al.* [31], where four efficient design variables in conjunction with the osculating cone theory were implemented into multi-objective optimisation, paves the way for a general optimisation framework for the aerodynamic shape optimisation of waveriders. A key feature of their approach is the validity of the input design parameters, a topic which has also recently been explored by Ghosh *et al.* [76].

An outstanding challenge of waverider optimisation is the creation of comprehensive software solutions which can take into account all aspects of the flight corridor. Specifically, optimisation methods to date struggled to integrate and balance aerodynamic, structural, and heating requirements. Furthermore, waverider optimisation is lacking a clearly defined design space. For example, the adjoint solver, as integrated in commercial software like Simcenter Star-CCM+ [77], provides detailed control over the vehicle shape but, as a result, is very likely to get stuck in local optima and prevent a thorough exploration of the parameter space [69]. To overcome such limitations, Son *et al.* [31] proposed a direct design method and a robust geometry parametrisation building on the works of Kontogiannis *et al.* [30] and Takashima and Lewis [26].

The starting point of the present study is the independent reproduction of the parametrised geometry generation and optimisation proposed by Son *et al.* [31]. Thereafter, the design space is explored and single-objective and multi-objective optimisation are carried out. To this end, a genetic algorithm is employed with a surrogate model derived from inviscid CFD data. The parametric waverider generation method as described by Son *et al.* [31] allows consideration of the wide-speed problem implicitly via an additional Mach number dependency which can then be leveraged in an optimisation framework. The adoption of such strategy is presently assessed. It differs from the more traditional approach to extend the efficient applicable range of a starting waverider geometry through various design methods such as combining two waveriders into one as explained by Zhao *et al.* [28]. An open-source Python software for the generation of the hypersonic waveriders has been developed [78,79] as part of this work with the aim to boost research in the field, often limited by the unavailability of geometry generation tools.

This work is structured as follows. Section 2 introduces details of the parametrised waverider geometry generation, CFD simulations, parameter space sampling, surrogate modelling, and optimisation methods. Section 3 presents design feature analysis, single-objective and multi-objective optimisation results alongside the discussion and outlines limitations of the presented work. Finally, conclusions are drawn in Section 4 and points for future research are highlighted.

2. Methods

This section provides a description of the proposed framework for waverider design optimisation depicted in Fig. 1. An initial design space sampling (see 2.3) of the selected design parameters is performed which is used to obtain a set of waverider geometries via an open-source generator (see 2.1). The computational mesh and setup for CFD analysis is subsequently performed (see 2.2) and the CFD simulations launched. Quantities of interest from the CFD runs are extracted (see 2.2) and surrogate models for each are built (see 2.3). These models are then used for single-objective and multi-objective shape optimisation studies with a genetic algorithm (see 2.4). Furthermore, a feature analysis of the design space inputs on the extracted quantities of interest is performed and discussed in the Results and Discussion section (3.1). This study is complemented by a thesis [79] and a public software repository[1] providing every detail underpinning this study to maximise reproducibility.

The Methods section is further structured as follows. The direct parametrisation method is introduced in Section 2.1. The CFD strategy and the associated surrogate modelling are detailed in Sections 2.2 and 2.3, respectively. Finally, the optimisation algorithm is covered in Section 2.4.

2.1. Waverider parametrisation

In this work, the parametrisation by Son *et al.* [31] is adopted to parametrise the base plane of the waverider (see Fig. 5 of Nassif [79] for an overview of typical waverider nomenclature). The technique makes use of four geometric parameters to define the upper surface curve (USC) and the shock wave curve (SC) of the waverider. This method consists of a small number of design variables while resulting in a wide variety of shapes (see Fig. 7 of Son et al. [31]), making it an efficient parametrisation method for optimisation. Fig. 2 describes the parametrisation scheme accounting for symmetry. A local two-dimensional coordinate system is set up such that $y' = y + h$, $z' = z$ and w represents the half-width of the waverider.

The SC is composed of a flat region, defined by the distance d_1, and a curved region following it. The curved region is defined as a fourth-order Bézier curve with five control points. These are equally spaced in z and lie on the line $y' = 0$, except for the rightmost whose vertical position is determined by the distance d_2. Furthermore, the USC is defined as a third-order Bézier curve with four control points. These are also equally spaced in z, while the vertical positions of the two internal points are determined by the distances d_3 and d_4. These distances are

[1] https://github.com/jade5638/jade_nassif_thesis

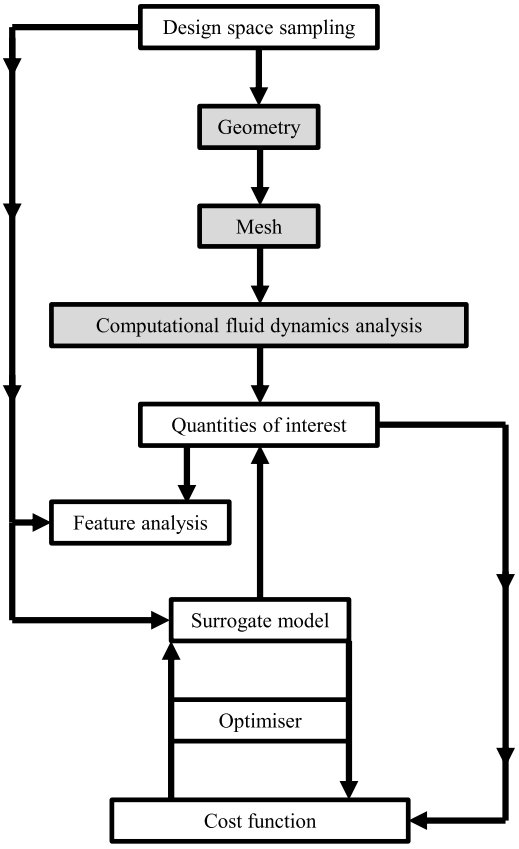


Fig. 1. Schematic of the proposed waverider optimisation framework inspired by the work of Son *et al.* [31]. The grey boxes are part of the flow field analysis whereas other steps are needed to tackle the optimisation problem.

then normalised as

$$\begin{cases} \text{X1} = \dfrac{d_1}{w} & \text{with } d_1 \in [0, w[& \rightarrow & \text{X1} \in [0, 1[\\ \text{X2} = \dfrac{d_2}{h} & \text{with } d_2 \in [0, h] & \rightarrow & \text{X2} \in [0, 1] \\ \text{X3} = \dfrac{d_3}{(h - d_2)} & \text{with } d_3 \in [0, h - d_2] & \rightarrow & \text{X3} \in [0, 1] \\ \text{X4} = \dfrac{d_4}{(h - d_2)} & \text{with } d_4 \in [0, h - d_2] & \rightarrow & \text{X4} \in [0, 1] \end{cases} \tag{1}$$

which gives the final four geometric parameters (X1, X2, X3, X4).

Sobieczky's [23] osculating cone method (see also [24] for a recent review) is then applied on the base plane to obtain the remainder of the waverider geometry.

The open-source "Waverider Generator" [78] Python package ensures the reproducibility of the geometry generation by integrating the Osculating Cone Theory (OCT) and the aforementioned parametrisation. It was used to produce all geometries in this work. A comprehensive description of the input geometrical and flow parameters is provided in Nassif [79] as well as more details on the OCT with appropriate references.

Son *et al.* [31] made use of the geometric parameters X1 to X4 to define a design space for optimisation as

$$\mathbf{V} = \begin{cases} \text{X1} \in [0, 1[\\ \text{X2} \in [0, 1] \\ \text{X3} \in [0, 1] \\ \text{X4} \in [0, 1] \end{cases} \quad \text{with respect to GC} : \quad \frac{\text{X2}}{(1 - \text{X1})^4} < \frac{7}{64}\left(\frac{w}{h}\right)^4. \tag{2}$$

Here $\mathbf{V}$ is the design parameter vector and GC refers to a Geometric Constraint. The rest of the parameters including h, w, M_{design}, and the β shock angle are kept constant.

A known problem in waverider generation through inverse design methods is the selection of the local curve radii of the SC which can lead to unfeasible geometries. Prior work from Kontogiannis [80] mentioned these radius curvature issues which had to be tackled through additional constraints as also acknowledged by Son *et al.* [31] Radius curvature issues are addressed here by the Geometric Constraint (GC) in Eq. (2) originating from OCT ensuring that the inverse design method does not fail. Specifically, the OCT requires the intersection between any two osculating planes to be above the USC [31].

As such, the GC dynamically restricts the maximum value that X2 can take based on the value of X1.

The same design space will be used in this study, with the addition of the design Mach number M_{design} as a design variable. This is because the optimisation problems considered here are multi-point and aim to optimise the performance of the waverider across two flight conditions.

The rationale behind the inclusion of M_{design} in the design space is that a waverider designed for Mach 5 will not maintain the design shock wave shape at Mach 8 and vice versa. For this reason, in this optimisation framework, the influence of M_{design} on the shock wave shape is considered. It is an inherent part of the wide-speed problem mentioned in Section 1. Fig. 3 shows the shock angle at the symmetry plane, denoted as β_0, against M_{design} for both flight conditions. Here, the design shock angle is $\beta = 15°$. The curves are obtained by making use of the oblique shock relations ($\beta - \theta - M$ relation).

At Mach 5, a waverider designed for that flight condition will have $\beta_0 = \beta = 15°$. Similarly, at Mach 8, a waverider designed for that flight condition will display $\beta_0 = \beta = 15°$. However, when the freestream Mach number $M_\infty \neq M_{\text{design}}$, the resulting β_0 is either higher (Mach 5) or lower (Mach 8) than the target. For simplicity and consistency across a range of waverider shapes, the change in the shock wave shape can therefore be quantified as:

$$\Delta\beta = |\beta_0 - \beta| \tag{3}$$

where β is the target shock angle. At $M_{\text{design}} \approx 6.1$, $\Delta\beta$ is equal for both flight conditions, and this can serve as an important point to compromise between the two design conditions. Furthermore, it's important to note that M_{design}'s contribution to the geometrical properties of the waverider is an increase in the deflection angle with an increase in M_{design}, as predicted by the $\beta - \theta - M$ relation. This translates to an increase in the thickness of the waverider for a specific shock wave shape. An example is shown in Fig. 4, where this phenomenon is clearly visible:

Presently, M_{design} is added to the design space of Son *et al.* [31] to give the final design space used in this study:

$$\mathbf{X} = \begin{cases} M_{\text{design}} & \in [5, 8] \\ \text{X1} & \in [0, 1[\\ \text{X2} & \in [0, 1] \\ \text{X3} & \in [0, 1] \\ \text{X4} & \in [0, 1] \end{cases} \quad \text{with respect to} \quad \begin{cases} \text{GC} : \frac{\text{X2}}{(1-\text{X1})^4} < \frac{7}{64}\left(\frac{w}{h}\right)^4 \\ \beta = 15° \\ h = 1.876 \text{ m} \\ w = 4.2 \text{ m} \end{cases} \tag{4}$$

where $\mathbf{X}$ is the vector of design variables. Including the design Mach number in this parameter set does allow the consideration of waverider geometries optimised for another Mach number than the ones of interest (5 and 8 in our case) and therefore increases the pool of potential shapes. The above set of parameters leads to a vehicle length $l = h/\tan(\beta) \approx 7$ m which is chosen to be similar to the X-51 [2] that is 7.5 m long.

The GC (see Eq. (4)) limits the maximum value that X2 can take as a function of X1. By denoting the RHS of the GC as a constant k, X2_{max} can be calculated as:

$$\text{X2}_{\text{max}} = \min\left(1, k(1 - \text{X1})^4\right) \tag{5}$$

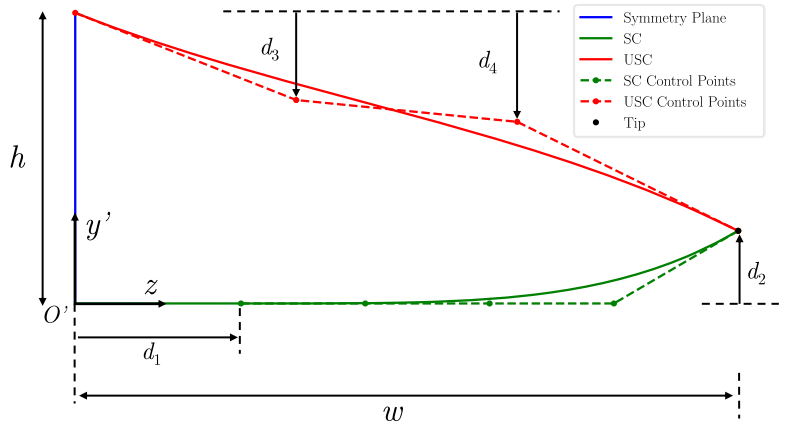


Fig. 2. Parametrisation of the base plane.

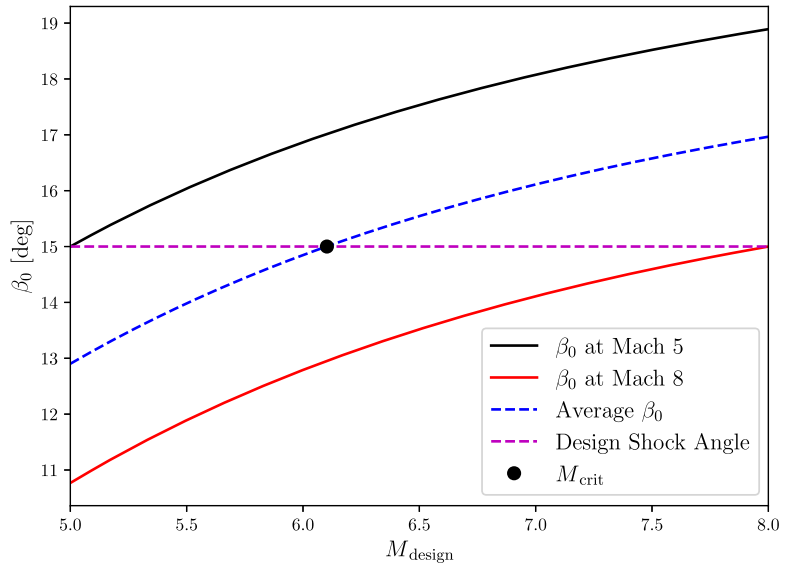


Fig. 3. Shock angle at symmetry plane against M_{design}.

As shown in Fig. 5, when X1 $\leq$ X$_{\text{crit}}$, X2 is not limited and can take any value between 0 and 1. After that point, X2$_{\text{max}}$ is less than 1 and decreases quartically. Note that throughout this work, k is multiplied by 0.9 to prevent floating-point errors during the optimisation process, and this is in line with the work by Son *et al.* [31]. In addition to the GC, the design space established in the previous section exhibits intricate relationships between the variables because of the parameter X2. Indeed, as seen in Eq. (1) and Fig. 2, the parameters X3 and X4 are coupled to X2 such that, as X2 increases, their influence on the geometry decreases. Ultimately, when X2 $= 1 \Rightarrow d_2 = h$, X3 and X4 become redundant as the distances d_3 and d_4 will be calculated as

$$\begin{cases} d_3 = \text{X3} \cdot (h - d_2) = \text{X3} \cdot 0 = 0 \text{ m} \\ d_4 = \text{X4} \cdot (h - d_2) = \text{X4} \cdot 0 = 0 \text{ m} \end{cases} \tag{6}$$

which will result in the same geometry regardless of the values of X3 and X4. This configuration corresponds to a waverider with a flat USC. Hereafter, X3 and X4 will be treated as 0 whenever a solution with X2 = 1 is reached to denote this specific case. It can be written in terms of **X** as:

$$\mathbf{X}_{\text{Flat USC}} = \begin{pmatrix} M_{\text{design}} \\ \text{X1} \\ \text{X2} \\ \text{X3} \\ \text{X4} \end{pmatrix} = \begin{pmatrix} M_{\text{design}} \\ \text{X1} \\ 1 \\ 0 \\ 0 \end{pmatrix} \text{w.r.t } \text{X1} \leq \text{X1}_{\text{crit}} \tag{7}$$

Additionally, setting X2 = 0 results in a planar shock wave. As a consequence, when X2 = 0, X1 becomes redundant as the entirety of the SC is already flat. Similar to the previous case, this case will be denoted hereafter as:

$$\mathbf{X}_{\text{Flat SC}} = \begin{pmatrix} M_{\text{design}} \\ \text{X1} \\ \text{X2} \\ \text{X3} \\ \text{X4} \end{pmatrix} = \begin{pmatrix} M_{\text{design}} \\ 0 \\ 0 \\ \text{X3} \\ \text{X4} \end{pmatrix} \tag{8}$$

Having established the inputs of the design space, many outputs of interest can be obtained, some of which are used in the optimisation problems. A database containing these outputs for 100 points across the design space was created and stored in this project's GitHub Repository[2].

[2] https://github.com/jade5638/jade_nassif_thesis

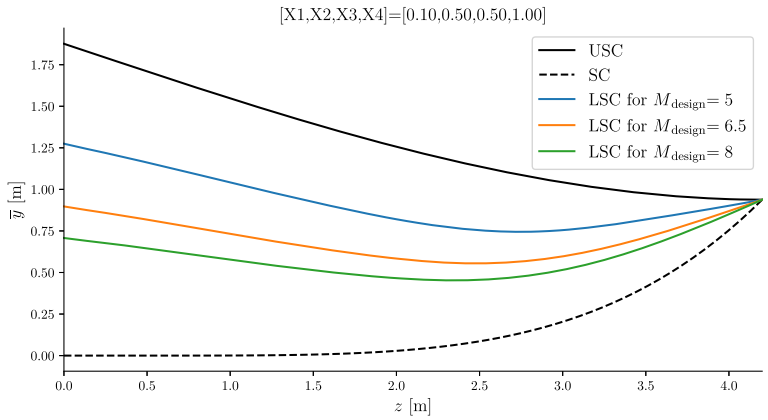


Fig. 4. Effect of M_{design} on the lower surface of the waverider. View from the base plane. For $\beta = 15°$, $h = 1.876$ m and $w = 4.2$ m.

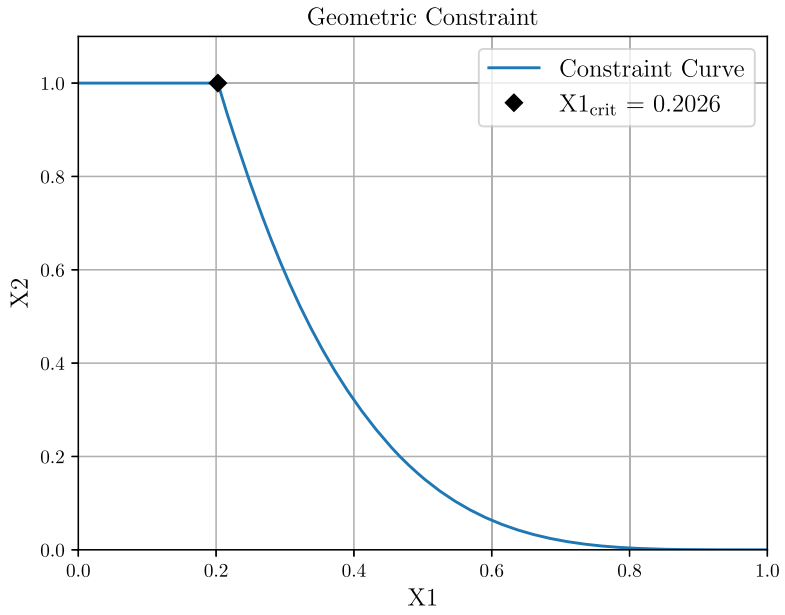


Fig. 5. Geometric constraint curve.

Table 1
Outputs of the design space.

Symbol	Unit	Output Description	Method
D	[N]	Inviscid drag force	Inviscid CFD
L	[N]	Inviscid lift force	Inviscid CFD
(L/D)	[-]	Inviscid lift to drag ratio	Inviscid CFD
V	[m^3]	Internal volume	`cadquery` [81]
S_{wet}	[m^2]	Wetted surface area	`cadquery` [81]
υ_{eff}	[-]	Volumetric efficiency	$V^{2/3}/S_{\text{wet}}$

The full sampling strategy is outlined later in Section 2.3. Table 1 lists the main outputs considered in this study and the methods by which these were obtained.

Note that, for convenience, all forces are those acting on only half the geometry as a symmetry plane boundary condition is applied in the CFD setup. Moreover, the lift and drag are obtained at angle of attack α of 0° representing cruise condition and this is the case throughout the optimisation. Furthermore, the subscripts "M5" and "M8" will be used hereafter to denote forces at the M5 and M8 flow conditions respectively. On the other hand, geometric properties such as V, S_{wet} and υ_{eff} are obtained on the entire geometry through `cadquery` [81], which is a Python library for handling and creating CAD models. The volumetric efficiency is presently computed with the wetted area which is readily available from cadquery. The literature favours the use of the planform area instead [17,82] which should be kept in mind when comparing with other work in the literature.

2.2. Performance estimation and computational setup

As shown in Table 1, the aerodynamic performance is obtained via CFD. This section describes the CFD setup used to solve the inviscid flow around a waverider with the Euler Equations. In this case, the flow is solved in a steady-state to represent cruising condition and minimise computational cost. The commercial CFD solver Simcenter STAR-CCM+ 19.02.009-R8 [77] was used to conduct all CFD simulations in this work, owing to its compact user interface which handles all stages of the simulation from meshing to post-processing. This feature, along with the use of Java macros, provides a significant advantage in terms of workflow automation. Throughout this section, the figures produced as well as the Grid Convergence Study were done on the waverider with

$$\mathbf{X} = (M_{\text{design}}, \text{X1}, \text{X2}, \text{X3}, \text{X4}) = (6.5, 0.25, 0.5, 0.5, 0.5)$$

which corresponds to the mid-range of each design variable - except for X1 as this would break the GC.

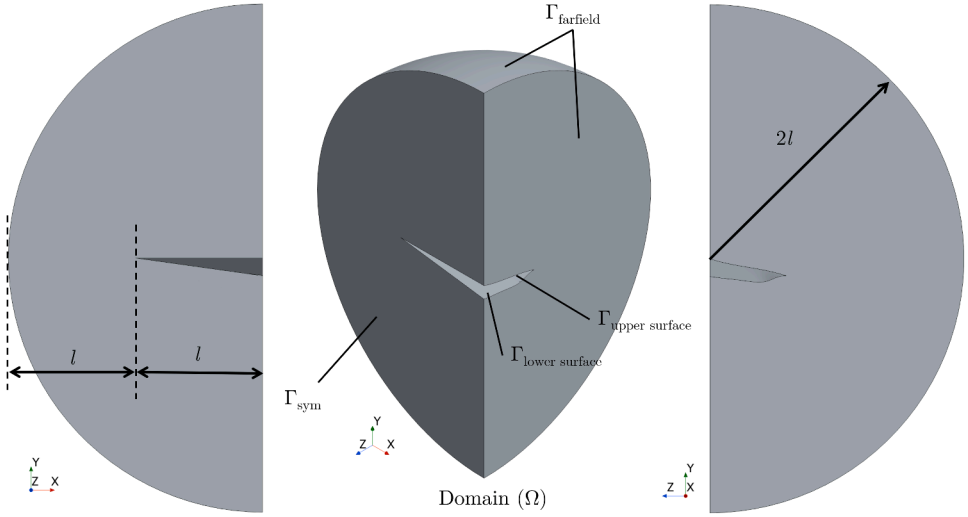


Fig. 6. Inviscid domain $\Omega \in \mathbb{R}^3$ used in this study, showing a view from the symmetry plane (left), isometric view (middle) and view from the back plane (right).

The domain presented in Fig. 6 was kept for all inviscid CFD simulations.

As is commonly done in the literature [31,44,74], the wake behind the waverider is not included in the domain due to the lack of viscosity which prevents an accurate representation of the wake and can lead to convergence issues. Furthermore, only half the body is included - making use of the symmetry. The boundaries of the domain $\partial\Omega$ have been divided into four regions such that:

$$\partial\Omega = \Gamma_{\text{farfield}} \cup \Gamma_{\text{sym}} \cup \Gamma_{\text{upper surface}} \cup \Gamma_{\text{lower surface}} \tag{9}$$

The mesh is unstructured and generated using Polyhedral elements with the built-in STAR-CCM+ automated mesher. Further details about the metrics used to obtain the base grids can be found in Nassif [79]. The shock wave is the main feature of the flow and is driving the lift and the drag characteristics. As such, Adaptive Mesh Refinement (AMR) was included in the CFD setup to ensure the sharp gradients around the shock are well captured and reasonable estimates of lift and drag are reached. The criterion chosen is shown in Eq. (10):

$$C = \|\nabla M(x,y,z)\| \cdot s = \sqrt{\left(\frac{\partial M}{\partial x}\right)^2 + \left(\frac{\partial M}{\partial y}\right)^2 + \left(\frac{\partial M}{\partial z}\right)^2} \cdot s \tag{10}$$

where $M(x,y,z)$ is the local Mach number represented as a scalar field across the domain and s is the Adaptation Cell Size (ACS), calculated as "twice the maximum distance between a cell centroid and any of the cell vertices" in Star-CCM+ [77]. The refinement can take place when $C \notin [0, 0.1]$, with a maximum refinement level of 2. Furthermore, the minimum Face Validity was set at 0.9 to prevent bad quality cells in the refined regions. Additionally, only cells with an ACS greater than 0.001 m were eligible for refinement. AMR was set to take place every 100 iterations to allow the solution on the current mesh to reach a realistic steady-state convergence before being refined. A number of refinements n_{ref} is also predefined to serve as a minimum number of iterations before considering the convergence criterion. For example, if $n_{\text{ref}} = 2$, then a minimum of $2 \times 100 = 200$ iterations is set before checking for convergence.

Fig. 7 showcases this AMR setup after 3 refinements at $\alpha = 0°$ for the M5 flow condition. The criterion is suitable for this type of flow as it successfully refines the region of the shock and the overflow to the upper surface. A grid convergence study is discussed in Nassif [79] for both the M5 and M8 cases and therefore it is not presented here.

Inviscid simulations were used to obtain the aerodynamic coefficients. The Coupled Implicit solver was selected where the equations get solved simultaneously through pseudo-time marching [77,83]. Moreover, the Advection Upstream Splitting Method (AUSM) + Flux Vector Splitting (FVS) [84] scheme was chosen to evaluate inviscid fluxes. In addition to this, the Courant number was determined through the Automatic Control method built into Star-CCM+ [77]. Furthermore, the Incomplete Lower Upper (ILU) [85] relaxation scheme was selected for the Algebraic Multigrid (AMG) Linear Solver. A third-order Monotonic Upstream-centred Scheme for Conservation Laws (MUSCL) scheme with central differencing was selected in conjunction with the Venkatatkrishnan [86] slope limiter. The scheme results in third-order accuracy except around regions with strong gradients, where the limiter reduces the accuracy to second-order [83]. Given the hypersonic nature of the flow, the air cannot be assumed to be an ideal gas [83,87]. For this reason, a Real Gas model known as Equilibrium Air [88], recommended by Cross *et al.* [83] and the Star-CCM+ user guide [77] was chosen. To complete this work, Cranfield University's High Performance Computing (HPC) facilities were used to run all CFD simulations. 16 cores were selected by default with a maximum time of one hour per simulation. In most cases, the computational time did not exceed 30–40 minutes. The choice of inviscid CFD simulations is mainly motivated by keeping the computational cost as low as possible as viscous simulations are at least an order of magnitude more expensive for the computational domain depicted in Fig. 6. Moreover, optimisation exercises are practically done using the cheapest available, but sufficiently accurate, method (inviscid CFD in this case) and the higher fidelity option is adopted for detailed design verifications and studies. This is exemplified by recent work [7,31,35] and motivates the current choice.

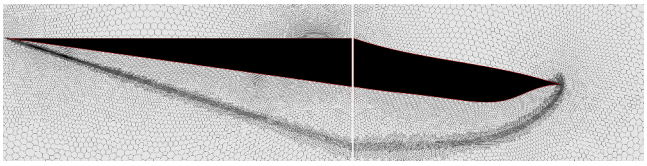


Fig. 7. AMR on the symmetry plane (left) and back plane (right) with $n_{\text{ref}} = 3$.

The lift to drag ratio L/D was chosen as a convergence criterion. This is because lift and drag are the two quantities which are obtained from the CFD setup and used in the optimisation problems, described in Section 2.4. The solution is considered converged if

$$\left|(L/D)_{\max} - (L/D)_{\min}\right| < \epsilon \tag{11}$$

Where $(L/D)_{\max}$ and $(L/D)_{\min}$ are the maximum and minimum values of L/D over 40 sequential samples, and $\epsilon = 1 \times 10^{-6}$. A maximum number of iterations was also set at 1000. In the event that convergence is not reached, the behavior of L/D is observed. If the quantity seems to

Table 2
Flow conditions employed for optimisation.

	M5 at 25 km alt.	M8 at 30 km alt.
p_∞ [Pa]	2506	1169
U_∞ [m/s]	1490	2416
T_∞ [K]	221.65	226.65
ρ_∞ [kg/m^3]	3.940×10^{-2}	1.797×10^{-2}

oscillate about a certain value but does not settle enough to reach the established criterion, then the solution is still deemed valid and the last value of L/D is recorded.

As specified earlier in Section 2.1, the multi-objective optimisation problems consider two flow conditions:

1. Mach 5 at 25 km altitude (M5)
2. Mach 8 at 30 km altitude (M8)

The two flow conditions are summarised in Table 2.

2.3. Surrogate modelling

The first step in building a surrogate model is to determine a set of sample points to accurately represent the design space and which will be used to train the model. As such, a first discussion focuses on the sampling methodology and the following part focuses on the training and validation of the surrogate models used in optimisation through a Kriging approach. The Surrogate Modelling Toolbox (SMT) Python library [89] was chosen to conduct all the steps outlined in these sections, as it provides a wide range of tools and options to construct surrogate models.

The Latin Hypercube Sampling method [90] was selected to sample the design space due to its numerous advantages over classic random sampling (see detailed discussion in 2.5.1 of Nassif [79]). In the work by Son *et al.* [31], which considers the same design space with the exception of the design Mach number, a final set of 60 points were used to train the surrogate models for volume, C_D and C_L. However, the latter two displayed poor accuracy in some regions, which could be partly due to an insufficient number of points. For this reason, and given the addition of M_{design} in the design space, a target was set to sample 100 points.

Due to the Geometric Constraint (see Section 2.1) which dynamically restricts X2, 500 samples were initially obtained via Latin Hypercube Sampling and these were then filtered to only keep the ones which satisfy the constraint, resulting in 183 valid points. The K-Means clustering algorithm, as implemented in the Scikit-learn Python package [91], was then applied to select 100 representative points from this set. Each sampling point i, representing a waverider, will be refered to as Waverider i. Waverider 63 was omitted from the set due to meshing issues, leading to 99 final sample points. Slices of the sampling across the design space are shown in Figure 16 of Nassif [79].

An ordinary Kriging model was built for each of the following quantities: V (internal volume), S_{wet} (wetted area), L_{M5} (lift at M5), L_{M8} (lift at M8), D_{M5} (drag at M5) and D_{M8} (drag at M8).

The samples obtained via Latin Hypercube Sampling (see Section 2.3) were first separated into a testing (10 %) and a training (90 %) dataset. The KRG class of the SMT Python package [89] was then used to train the surrogate models, each instance of this class representing an individual surrogate model. The models were then evaluated on testing data with very satisfactory predictive behavior. For further details, the reader is referred to Nassif [79].

2.4. Shape optimisation

This section outlines the optimisation approach taken and the different cases considered. The implementation of the Genetic Algorithm (GA) used in the optimisation is first covered. Single-objective unconstrained test cases are then presented, the objectives of these being to:

- evaluate the performance of the surrogate model and optimisation algorithm on simple cases.
- identify redundant optimisation objectives.

Five multi-objective optimisation cases are finally presented.

Table 3
Summary of the considered optimisation cases.

Optimisation Case	Objective
1	Maximising volume
2	Maximising lift L_{M5}
3	Maximising volume & minimising inviscid drag

Across the optimisation cases, the cost function may be normalised with respect to a reference value for easier comparison across these cases. These values ($\overline{D}_{M5}$,$\overline{D}_{M8}$,$\overline{L}_{M5}$,$\overline{L}_{M8}$) are obtained as the averages across the database of samples and are summarised in Table 10 of Nassif [79].

Genetic algorithms (GA) [92], which mimic the process of natural selection, evolve a set of solutions over many generations. This makes them suitable for multi-objective problems with conflicting objectives, where a set of optimal trade-off solutions is more relevant than a single optimal solution. At every generation, "genetic" operations are applied on "parent" solutions to obtain new "offspring" solutions based on their performance (fitness value). This allows for a thorough exploration of the design space. The GA of the Python library PyGAD [93] was used in this work, owing to its flexibility and extensive documentation. It is worth noting that PyGAD maximises the solution, and so this may be reflected in the way the optimisation problems are tackled and presented hereafter. The following paragraphs outline the optimisation setup.

GAs are inherently random due to their stochastic processes. As such, the optimisation was run more than once to ensure robustness and consistency in the results. In multi-objective problems, after each run, the set of Pareto-optimal (non-dominated) solutions from the last generation was recorded. Once all the runs were performed, the set of non-dominated solutions across all runs was computed to give the final Pareto front. Further details about exact parameter settings are provided in Table 5 of Nassif [79].

Given that GAs cannot directly evaluate constraints, it was decided to indirectly account for broken constraints via a penalty approach with details found in Nassif [79]. Furthermore, to favour geometrically valid solutions, it was decided to attribute a fitness value of 0 whenever the Geometric Constraint (GC) is broken. This would prioritise valid solutions and minimise the number of non-valid solutions present at every generation.

Here, two single-objective cases and one multi-objective case are described as summarised in Table 3. These unconstrained optimisation cases were found sufficiently representative of the general capabilities of the approach. The cost function of lift maximisation (case 2 in Table 3) is simply $L_{M5}/\overline{L}_{M5}$. By comparison, formulating the multi-objective optimisation (case 3 in Table 3) is slightly more complicated based on

$$Maximise \begin{cases} V \\ 1/D_{\text{avg}} \end{cases} \tag{12}$$

where:

$$D_{\text{avg}} = \frac{0.5D_{\text{M5}} + 0.5D_{\text{M8}}}{0.5\overline{D}_{\text{M5}} + 0.5\overline{D}_{\text{M8}}}. \tag{13}$$

It is worth acknowledging that Eq. (13) can be extended to include transonic and supersonic flow conditions in the optimisation. In short, the proposed method provides freedom for customisation regarding wide-speed waverider design along trajectories of interest. The reader is referred to section 2.6.3 of Nassif [79] for the comprehensive analysis

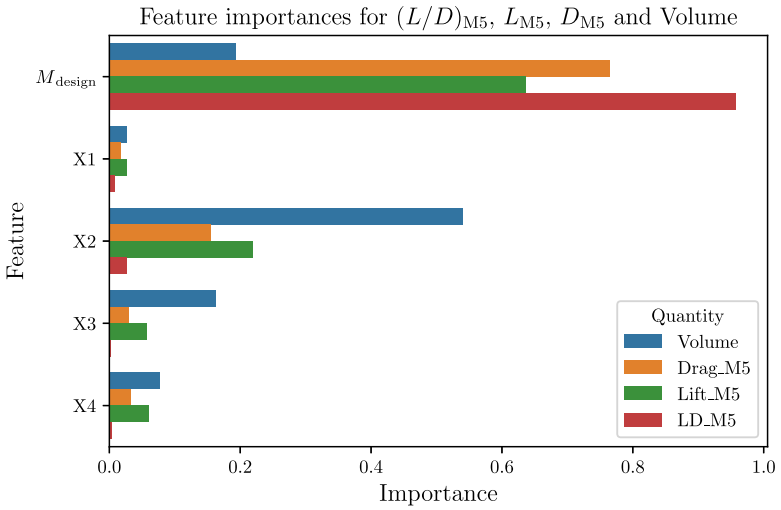


Fig. 8. Feature importances for $(L/D)_{M5}$, L_{M5}, D_{M5} and volume.

of further constrained and unconstrained single-objective and multi-objective optimisation cases.

3. Results and discussion

In Section 3.1, the importance of each design parameter is discussed based on single-objective optimisation results. Then, the single and multi-objective optimisation results are covered in Sections 3.2 and 3.3, respectively.

3.1. Design space analysis

Son *et al.* [31] made use of Analysis of Variance (ANOVA) to determine the influence of the inputs on the outputs of the design space. However, ANOVA assumes independence between the design variables. As demonstrated in Section 2.1, interdependencies do exist between the design variables, and this can lead to inaccuracies in the outcome of ANOVA. In this work, another approach was taken by training random forest models (RFMs) and extracting the feature importances. In a RFM, the importance of a feature directly reflects how crucial this feature is in correctly predicting the output, as it is calculated based on the feature's contribution to minimising error across the ensemble of decision trees [94]. Moreover, RFMs do not assume independence and are able to model complex relationships, making them a more suitable and flexible alternative to ANOVA. These models were trained solely for this purpose via the Scikit-learn Python package [91] with 1000 trees.

The feature importances are shown in Fig. 8 for M5. The M8 results do provide the same insight and are therefore not discussed here.

The $(L/D)_{M5}$ is clearly dominated by M_{design} with the other variables playing little to no importance in determining the ratio. Looking more closely at the available sample points in Fig. 12, M_{design} generally leads to a decrease in $(L/D)_{M5}$. The relationship is non-linear and appears to "cap" the maximum lift to drag ratio achievable as a function of M_{design}.

Similarly, L_{M5} and D_{M5} are mainly driven by M_{design}. From Fig. 9, an increase in M_{design} generally leads to an increase in L_{M5} and the same is shown in Fig. 22c of Nassif [79] for D_{M5}. However, the geometric parameters have gained more importance than with $(L/D)_{M5}$, especially in the prediction of lift. Furthermore, in the paper by Son *et al.* [[31], Fig. 9], X3 has significantly more influence on lift and drag compared to X4. Here, their importances are similar, and this may be a result of one, or a combination of (a) Larger number of samples, (b) Introduction of M_{design} to the design space, (c) Use of a RFM instead of ANOVA. When it comes to volume, X2 has the most influence on the output and is in line with the findings of Son *et al.* [31]. This is because X2 controls the curvature of the SC, which determines the location of the centre of the local osculating cone and therefore influences the flowfield the most [31]. As seen in Fig. 9, a higher value of X2 tends to result in a higher volume. This is in line with the findings of Son *et al.* [31] where the maximum volume waveriders found in the optimisation neared X2 = 1. Moreover, X3 is more important than X4, which is the opposite in Son et al. [31]. Once again, this may be attributed to one of the reasons mentioned earlier.

Table 4
Maximum and minimum volume values for three design Mach numbers.

M_{design}	V_{min} [m^3]	V_{max} [m^3]	ΔV [m^3]
5.0	2.54	13.31	10.68
6.5	4.11	21.02	16.91
8.0	4.91	24.90	19.99

Overall, the introduction of M_{design} to the design space reveals the major role it plays in determining key aerodynamic properties like L/D, lift and drag. This is because, for a combination of X1 to X4 (i.e., specific shock wave and upper surface shapes), M_{design} determines the upper and lower bounds of volume. Indeed, as mentioned in Section 2.1, an increase in M_{design} results in an increase in the deflection angle, which increases overall volume. With this in mind, the trade-off relationships between lift/drag and volume, identified in the previous section, explain why lift and drag tend to increase with M_{design}.

Furthermore, as seen in Fig. 9 for L_{M5}, as M_{design} increases, the range of lift also appears to increase (i.e., the difference between the maximum and minimum values). The same is seen for the D_{M5} in Fig. 22c of Nassif [79]. For a given M_{design}, the minimum volume waverider is obtained when:

$$\mathbf{X} = \left(M_{design}, \text{X1}, \text{X2}, \text{X3}, \text{X4}\right) = \left(M_{design}, 0, 0, 1, 1\right)$$

which corresponds to a flat SC with the lowest possible USC. On the other hand, the maximum volume waverider is obtained when:

$$\mathbf{X} = \left(M_{design}, \text{X1}, \text{X2}, \text{X3}, \text{X4}\right) = \left(M_{design}, \text{X1}_{crit}, 1, 0, 0\right)$$

Which corresponds to a SC with maximum curvature, flat USC and maximum flat section in the SC. The minimum and maximum volumes were recorded for three values of M_{design} and this is shown in Table 4. ΔV denotes the difference between the maximum and minimum.

Table 4 highlights the increase in ΔV with M_{design}. Therefore, this explains why the plots of lift and drag against M_{design} appear to "widen" with an increase in design Mach number.

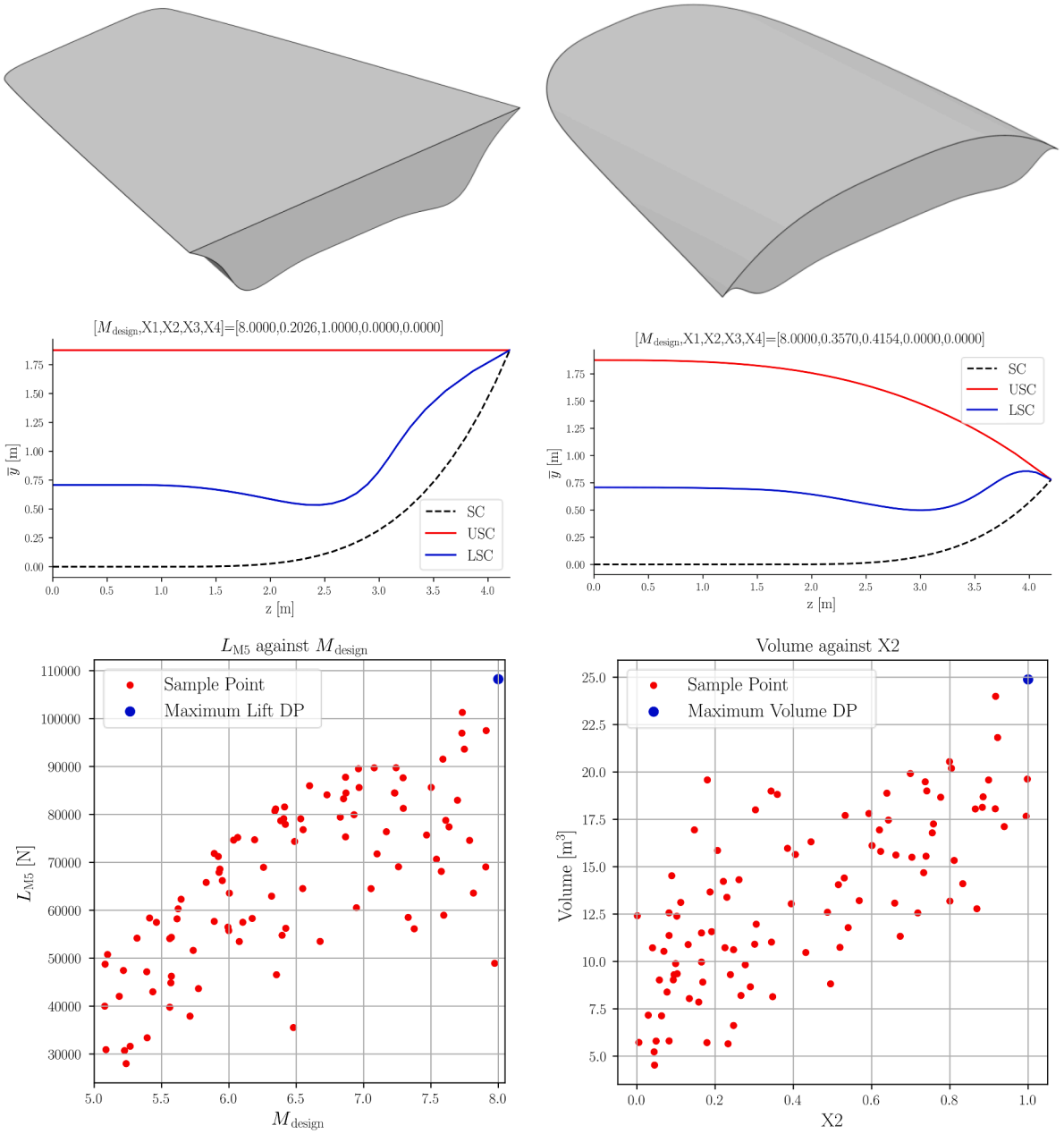


Fig. 9. Visualisation of the single-objective optimisation results with maximum volume (left) and maximum lift (right) as objectives. 3D view of two optima reached in the test cases (top) along with corresponding plots of the base plane (middle). Graph of the lift as a function of the design Mach number (left) and graph of the volume as a function of the X2 design parameter for all samples.

3.2. Single-objective optimisation cases

Fig. 9 presents the optimal solutions for the single-objective cases introduced in 2.4 which aim at maximising the volume and the L_{M5}. A scatter plot of the originally sampled design space used in creating the surrogate model and the surrogate predicted optimal solution is also provided for each objective function. The maximum volume case results in values for X2 of 1 and a design Mach number of 8. The behaviour is in line with the dominant identification of both these parameters on the volume as indicated in the feature analysis (3.1). X1 has reached its critical value and the values of X3 and X4 do not play a role any more as a flat USC is obtained (see discussion in 2.1). The maximum L_{M5} solution is also one where the design Mach number is 8 but unlike the other optimal solution, both X1 and X2 do play a role. The intersection of the USC and LCS is closer to the LSC value at the symmetry plane resulting in a more rounded USC. A posteriori CFD analysis of the optimal shapes did indicate relative errors in surrogate models predicted values below 1 % (see Table 16 of Nassif [79] for a quantitative overview). Overall, the optimisation setup's ability to successfully reach both known and unknown solutions with high accuracy has been demonstrated by these test cases.

3.3. Multi-objective optimisation case

The multi-objective case discussed here aims at maximising the Volume while minimising the drag. In this case, both Mach 5 and Mach 8 are considered relevant as defined in Section 2.4. Fig. 10 presents the resulting solutions as a Pareto front. The Drag Fitness (proportional to average drag cost function defined in Eq. (13)) as a function of Volume indicates the conflicting objectives and a suite of shapes are found

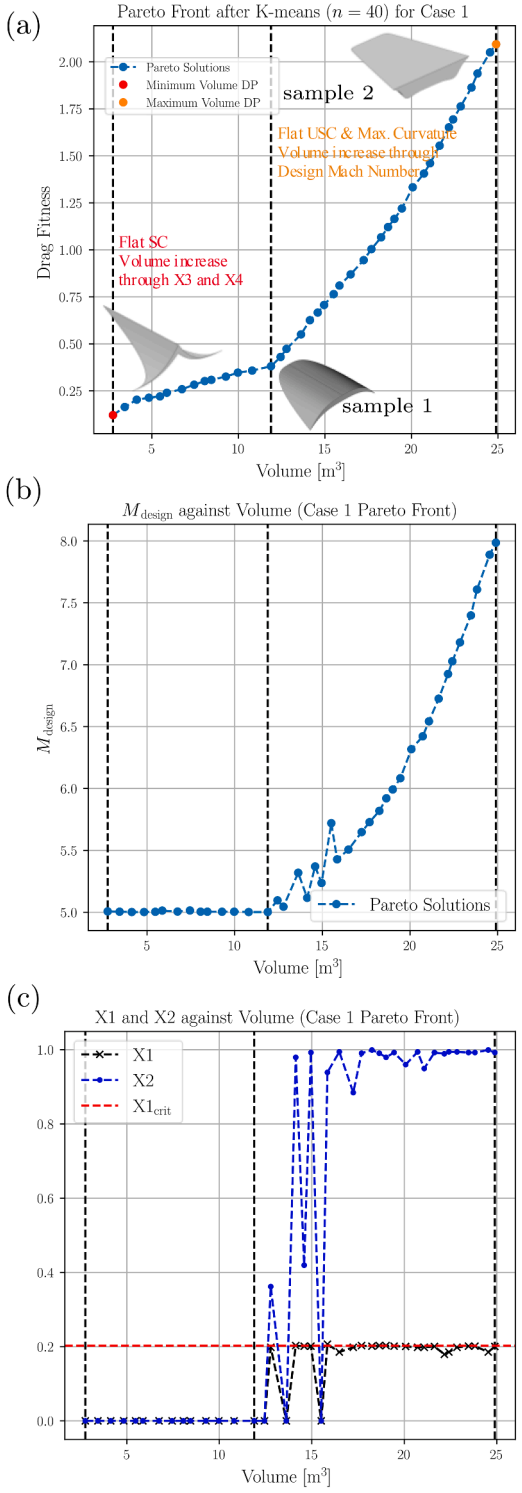


Fig. 10. Pareto front as function of the volume and the drag fitness (a). Pareto front as a function of the volume and the design Mach number (b). Design parameters as functions of the volume indicating two distinct geometries as the results of the optimisation (c).

which favour one objective over the other. In the Pareto Front obtained by Son et al. [31], the trade-off relationship is non-linear. Here, the relationship between the two appears linear with a first linear region that spans from the minimum volume to a volume of 12.5 m^3 while the second covers the remaining range till the maximum volume. These will be referred to as the first and second intervals hereafter. The role of M_{design} in shaping the waveriders is shown in the centre of Fig. 10. It

Table 5
Comparison between single-objective and multi-objective optimisation results.

Design Point	V [m^3]	L_{M5} [N]	D_{M5} [N]	$(L/D)_{M5}$
Case 1	24.96	104,073	19,499	5.3
Case 2	24.08	108,690	18,596	5.8
Pareto Sample 1	12.78	49,987	4704	10.6
Pareto Sample 2	24.89	103,847	19,455	5.3

can be seen that in the first interval, M_{design} remains more or less constant around 5. Then, it oscillates slightly until it starts stably increasing throughout the second interval. The two parts of the Pareto Front are visible through multiple outputs of the design space as discussed in Nassif [79]. Finally, the behaviour of X1 and X2 across the Pareto front is shown in the bottom panel of Fig. 10. During the first interval, both variables are zero, which corresponds to waveriders with a flat Shock wave Curve (SC). Then, a buffer/transition zone takes place until the variables stabilise into the second interval. In this second part, X2 tends towards its maximum value of 1 while X1 stabilises around $X1_{crit}$. When X2 reaches its maximum value, $X1_{crit}$ is the maximum value X1 can take according to the GC. For a given M_{design}, this configuration also represents the maximum volume waverider, as has been shown in 3.1. Along with the previous discussions, this further confirms the findings that:

- The Pareto Front is divided into two main linear regions. In the first region, the increase in drag is less steep than in the second.
- In the first region, $M_{design} \approx 5$ and a flat SC is favoured. Furthermore, $(L/D)_{M5}$ and v_{eff} do not vary much [[79], Fig. 25].
- In the second region, the maximum volume configuration for a given M_{design} is favoured. Additionally, M_{design} increases rapidly while $(L/D)_{M5}$ decreases rapidly [[79], Fig. 25] and Fig. B.16.

Furthermore, this division in the Pareto Front shows that, in the first section, the increase in volume is provided by a change in the shape of the USC - given that the SC is flat and M_{design} is constant. On the other hand, in the second section the increase in volume is provided purely by an increase in M_{design}. With regards to the Pareto Front, this indicates that the flat SC configuration can provide a sufficient increase in volume early on and maintain a low drag. However, at some point a steep increase in drag becomes inevitable if an increase in volume is to be achieved and so the solution then shifts to the second section of the Pareto Front with the increase in M_{design}.

A comparison between sample results of the Pareto front and the Single objective Case 1 (maximise volume) and 2 (maximise L_{M5}) is presented in Table 5. Pareto Sample 1 is a point just to the right of the line delimiting the left zone to the right zone while Sample 2 corresponds to the upper right point in Fig. 10 (a). The waverider shapes for Single objective Case 1 and Pareto Sample 2 are very similar indicating the equivalence of the objectives. Single objective Case 2 is a shape that can be found towards the right end of the Pareto front and is associated with high drag and lower aerodynamic efficiency. Pareto Sample 1 illustrates the compromise between payload and aerodynamic efficiency (range).

Fig. 11 presents the inviscid flow fields predicted with CFD for geometries number 67 ($M_{design} = 5.1$) and 42 ($M_{design} = 7.7$) from the original database used in the surrogate model. These geometries are representative for the two extremities of the Pareto front with the former one being a low volume flatter shock surface case and the latter being a high volume case with curved shock. The flat shock waverider design does not show signs of spillage at off-design (see (a) and (b)) unlike the other (see (c) and (d)) geometry and is indicated clearly by the density gradients. The magnitude of the pressure coefficient on the lower surface of waverider 42 is higher than waverider 67 which results in higher absolute lift force. However, as previously explained, the growth in volume increases the drag force significantly leading to smaller overall L/D.

One aspect observed with the introduction of M_{design} into the design space is a limited diversity in the resulting geometries. In the present

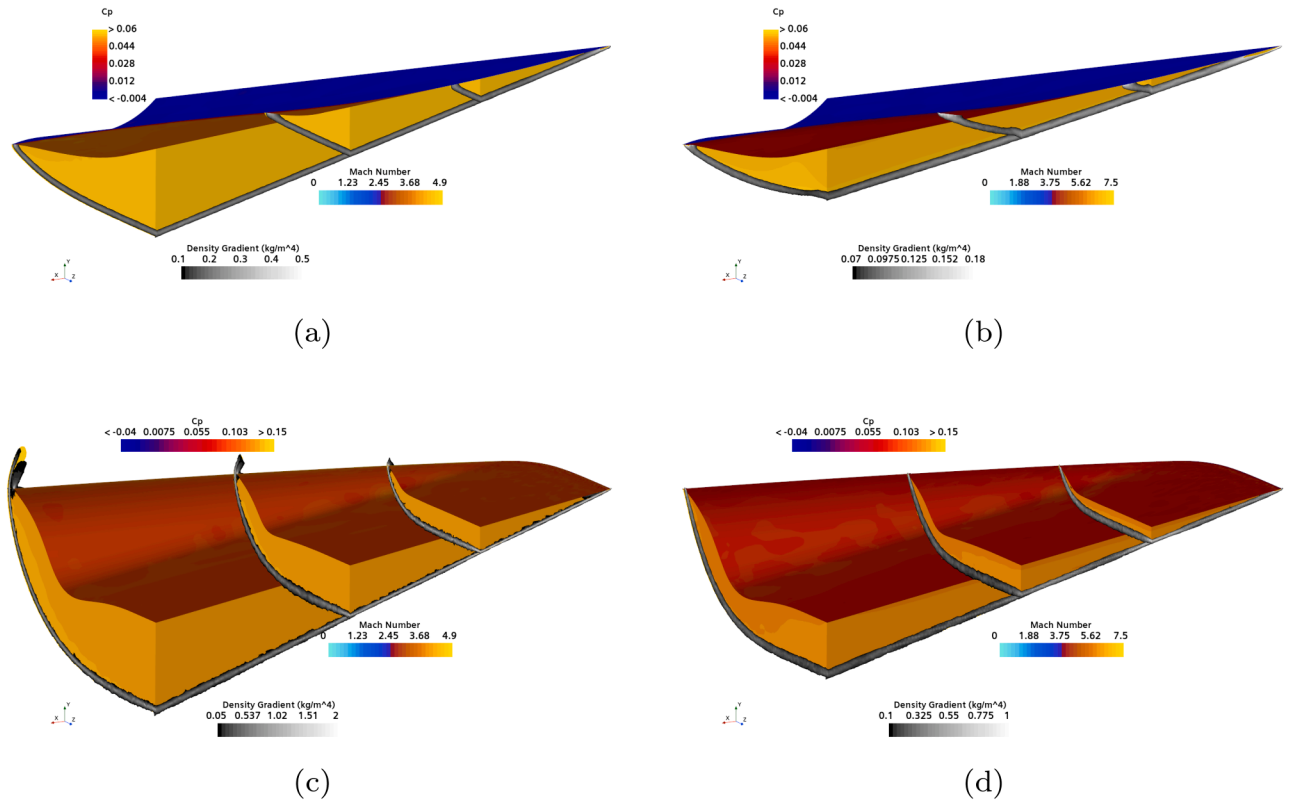


Fig. 11. Flow field contours of Mach number and density gradient as well as surface pressure coefficient: geometry 67 at (a) Mach 5, 25 km, and (b) Mach 8, 30 km; geometry 42 at (c) Mach 5, 25 km, and (d) Mach 8, 30 km condition. The same focal point is applied for these visualisations. Three axial cuts are shown with flow going from right to left.

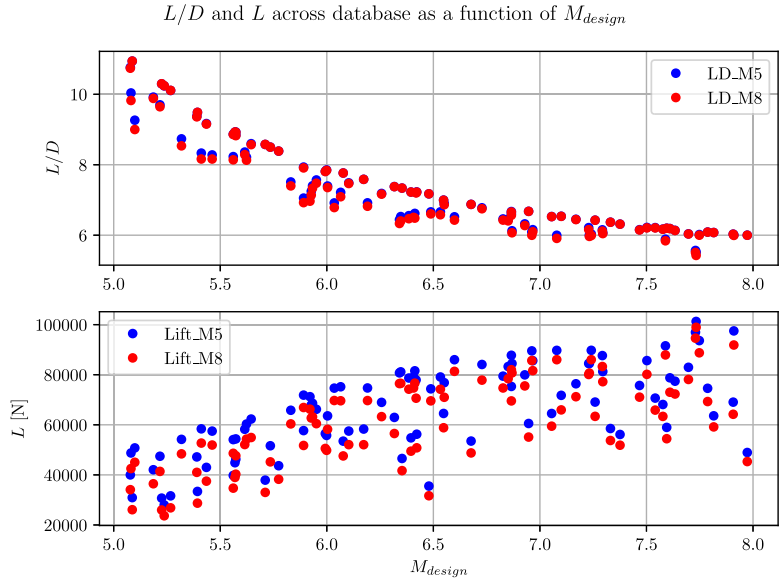


Fig. 12. $(L/D)_{M5}$, $(L/D)_{M8}$ (top) and L_{M5}, L_{M8} (bottom) as a function of M_{design} across the sampled points.

study, only two distinct waverider configurations were obtained. Indeed, only two "types" of waveriders were presently obtained. Son *et al.* [31] fixed the design Mach number and performed optimisation only through the geometric parameters X1…X4. Their resulting shapes progressively change through the Pareto Front. Introducing M_{design} may prevent such a diverse set of solutions from being reached. This is likely because an increase in volume can also be obtained via M_{design}. Whereas, when M_{design} is constant, the increase in Volume can only be achieved via the manipulation of the geometric parameters, yielding a Pareto Front similar to the one reported in Son et al. [31]. Narrowing down the parameter space can ease optimisation, however, the final shape is not solely determined by aerodynamic variables but a multitude of other engineering subdisciplines such as potential intake integration, stability and control, structures and mass balance, trajectory optimisation and heat management as exemplified by Bowcutt [33].

3.4. Limitations

There are several limitations associated with the present work which are briefly discussed here. Regarding the input design space variation, currently the parameters X1 to X4 are sampled between [0,1] (see Section 2.1). The multi-objective optimisation results indicate a range of optimal shapes with a flat SC which do not allow for practical internal volume usage (caret waveriders). Further efforts are needed to limit the design space input parameter ranges to avoid these shapes allowing for more practical designs. This engineering practicality has to be linked with internal system design and control surface sizing. Furthermore, viscous heating should be considered to devise the heat management and / or thermal protection which requires viscous CFD simulation and blunt leading edges. If a wider variability of waverider shapes is of interest, a different parametrisation might be more suitable as presently the design space is dominated by M_{design} limiting the type of results. This can be done within the current open-source framework.

Another point of interest, mentioned in the present work, is the possibility to rely on a viscous correction to modify inviscid drag coefficients as a low-cost solution and consider it in potential objective functions. The feasibility of such an approach has been demonstrated in the literature for the STRATOFLY MR3 waverider configuration [35]. Furthermore, a similar strategy has been adopted in the trajectory optimisation work on the GHGV-2 waverider configuration as mentioned in Autenrieb and Fezans [7]. This exercise, for the waverider shapes herein presented, is left for future work but the applicability of such a strategy is demonstrated in Appendix A.

The presented multi-objective case relies on the volume instead of the volumetric efficiency. Explorations with the volumetric efficiency as a cost function (see [79] 3.3.2.2 on page 68) have shown jumps and gaps in the pareto front indicating poor coverage of the objective as a function of other outputs such as drag. The result is attributed to the non-linearity of the cost function itself and further investigations are required such as extending the surrogate model database.

4. Conclusions

An approach for the aerodynamic shape optimisation of hypersonic waveriders, based on the reference framework by Son *et al.* [31], was further explored in this work. The approach made use of a geometric parametrisation (X1,X2,X3,X4) of the back plane in conjunction with the osculating cone theory providing valid geometries. To perform design-space exploration studies, inviscid CFD simulations were used for performance estimation, and an accurate Kriging surrogate model was trained for outputs of interest. A genetic algorithm was then coupled to the surrogate models and used to perform optimisation.

Feature importances analysis via random forest models indicates that the design Mach number is the driving factor for L/D, lift and drag. In particular, M_{design} appears to heavily influence the behaviour of L/D. Volume remains primarily controlled by X2 due to the curvature of the shock wave playing the biggest role in the volume of the vehicle.

Single-objective optimisation test cases were then performed to assess the accuracy of the surrogate and the performance of the overall optimisation setup. These confirmed the major role of the design Mach number in shaping the optimal waveriders for their respective objective function.

A multi-objective multi-point case with conflictive objectives of maximising volume while minimising drag was presented. The Pareto Front of solutions consists of two linear regions. In the first region, the optimisation favours solutions with a flat shock wave shape and a fixed design Mach number. In the second region, M_{design} begins increasing while favouring various solutions with a flat upper surface, maximum curvature, or a maximum flat shock region ($X1 = X1_{\text{crit}}$).

Overall, this work establishes an openly available and extensible optimisation framework that enables systematic and computationally tractable exploration of waverider design spaces. By combining surrogate modelling, genetic optimisation, multi-Mach-number simulations and cost function engineering, the study provides a reproducible foundation for scalable and generally applicable product development. Various points for future work can be considered. This includes the use of viscous simulations to tune the viscous correction coefficients adopted in this work which might depend on shape families. The design-space exploration tasks could also include static aerodynamic stability considerations to make it more practical. Design space explorations could be made for vehicles with different size ranges which could potentially identify similarities.

CRediT authorship contribution statement

Jade Nassif: Writing - original draft, Visualization, Validation, Methodology, Investigation, Formal analysis; **Jimmy-John OE Hoste:** Writing - review & editing, Supervision, Software, Methodology, Investigation, Data curation, Conceptualization; **Tamás István Józsa:** Writing - review & editing, Supervision, Resources, Project administration, Data curation, Conceptualization.

Data availability

Complementing data is available from GitHub and the developed software is stored here.

Declaration of competing interest

The authors declare that they have no known competing financial interests or personal relationships that could have appeared to influence the work reported in this paper.

Acknowledgments

The authors would like to thank Marc Famada Vizcaino of Destinus and Alberto Simón Félix of Capgemini for valuable discussions during their MSc studies at Cranfield University.

Appendix A. Viscous correction

The use of visous corrections for modifying inviscid drag resulting from affordable CFD simulations as an alternative to more costly fully viscous simulations has been adopted in the waverider literature [7,35]. Ding *et al.* [95] present visous drag contributions between 10 and 35 % for Mach 4, 6 and 8 flows at various angles of attack. In the work of Viole *et al.*, viscous drag contributions in the order of 20 to 30 % are observed (inferred from available plots) between Mach 4 and Mach8 at 0 deg angle of attack. The visous correction adopted in the latter work is given by Eq. (A.1).

$$\Delta C_{D,\text{visc}} = \alpha \left[\log_{10}\left(L_{\text{ref}}\,\text{Re}_{\text{unit}}\right)\right]^{-2.58}\left(1+\beta M^2\right)^{-\gamma}\frac{S_{\text{wet}}}{S_{\text{ref}}} \tag{A.1}$$

The formula relies on the reference length, the unit Reynolds number, the Mach number, the wetted area and the reference area. There are three tuninig coefficients which are fitted to $\alpha = 0.43$, $\beta = 0.31$ and $\gamma = 0.37$ for the STRATOFLY MR3 vehicle.

To confirm the applicability of the viscous correction formula of Eq. (A.1) to the present work, a similar fitting exercise is performed. To this end, waverider number 67 (Fig. A.13) from the surrogate database [3] is selected as it presents the highest L/D case for both Mach 5 and Mach 8 with a value of ≈ 11 and corresponds to the upper right most point of Fig. A.14.

The fitting is performed based on five Mach number cases (Train set) computed with the same cut-back configuration as in Section 2.2. An altitude of 30 km is considered for these cases resulting in different

[3] https://github.com/jade5638/jade_nassif_thesis

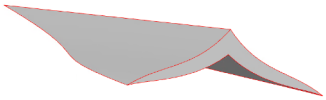


Fig. A.13. Waverider number 67 of database used for surrogate model.

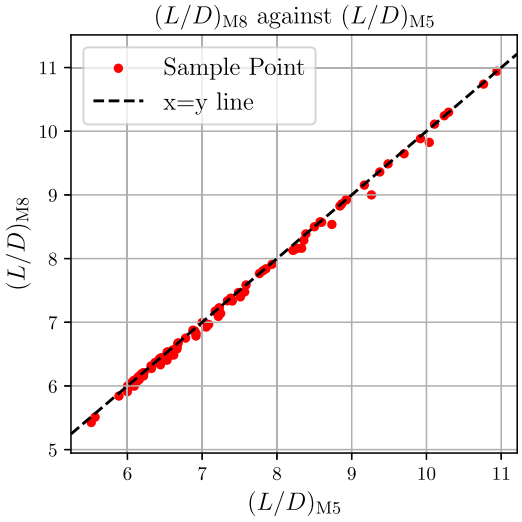


Fig. A.14. Inviscid L/D Mach 5 vs Mach 8 for surrogate samples.

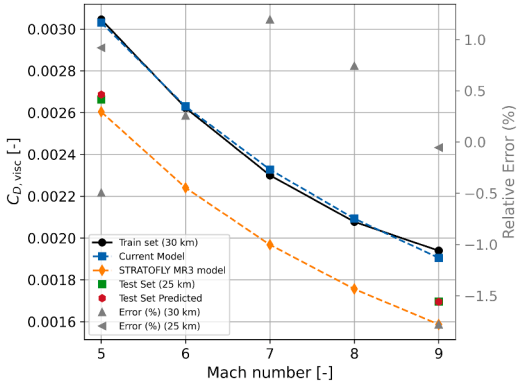


Fig. A.15. Viscous correction evaluation for waverider number 67.

Reynolds numbers. In addition, two other cases have been computed at an altitude of 25 km for both Mach 5 and Mach 9 and are used for a posteriori checking purposes of the fitted coefficients (Test set). The viscous contributions obtained from the various simulations range between 38 - 42 %. The least squares regressor of the Scipy Python library is used for the fitting with lower bounds set to 0 and without upper bounds. Fig. A.15 presents the result of this exercise which resulted in tuning coefficients $\alpha = 0.538$, $\beta = 0.516$ and $\gamma = 0.332$. The STRATOFLY MR3 viscous correction is also presented and is clearly under-estimating the viscous contribution for this specific waverider which is not unexpected as presently no wake is considered. The relative errors between actual viscous drag predictions and viscous corrections are below 2 % in absolute value for both train and test sets. These results illustrate the feasability of relying on a viscous correction form of the like of Eq. (A.1)

Appendix B. L/D as a function of M_{design} across Pareto front

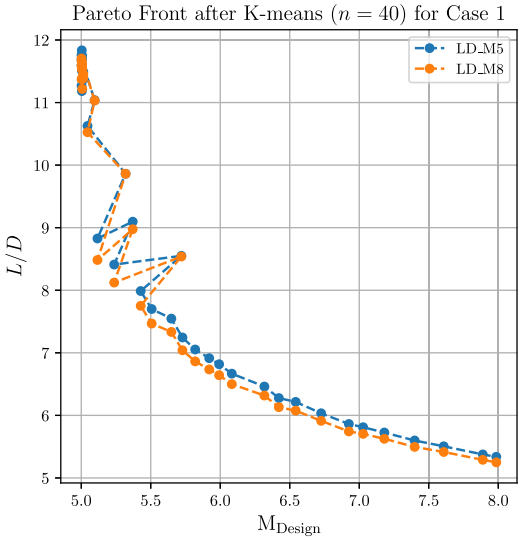


Fig. B.16. L/D as a function of M_{design} across the optimised geometries.

References

[1] C. McClinton, X-43-scramjet power breaks the hypersonic barrier: Dryden lectureship in research for 2006, in: 44th AIAA Aerospace Sciences Meeting and Exhibit, 2006, p. 1.

[2] J. Hank, J. Murphy, R. Mutzman, The X-51A scramjet engine flight demonstration program, in: 15th AIAA International Space Planes and Hypersonic Systems and Technologies Conference, 2008, p. 2540.

[3] S. Walker, J. Sherk, D. Shell, R. Schena, J. Bergmann, J. Gladbach, The DARPA/AF falcon program: the hypersonic technology vehicle# 2 (HTV-2) flight demonstration phase, in: 15th AIAA International Space Planes and Hypersonic Systems and Technologies Conference, 2008, p. 2539.

[4] M. Zhang, L. Xia, K. Zhao, L. Shi, R. Zhang, Y. Zhu, J. Deng, Aerodynamic and stealth integrated design of hypersonic vehicle based on discrete adjoint method, Aerosp. Sci. Technol. 162 (2025) 110222.

[5] K. Bowcutt, A. Paull, D. Dolvin, M. Smart, Hifire: an international collaboration to advance the science and technology of hypersonic flight, in: Proceedings of the 28th International Congress of the Aeronautical Sciences, ICAS Secretariat RA Leiden, The Netherlands, 2012, pp. 2012–2998.

[6] S. Di Benedetto, M.P. Di Donato, A. Rispoli, S. Cardone, J. Riehmer, J. Steelant, L. Vecchione, HEXAFLY-INT project: design of a high speed flight experiment, Proceedings of ISHF (2017).

[7] J. Autenrieb, N. Fezans, Flight control design for a hypersonic waverider configuration: a non-linear model following control approach, CEAS Space J. (2024) 1–24.

[8] F. Ferguson, M. Dhanasar, I.M. Blankson, Waverider design and analysis, in: 20th AIAA International Space Planes and Hypersonic Systems and Technologies Conference, American Institute of Aeronautics and Astronautics, Reston, Virginia, 2015. https://doi.org/10.2514/6.2015-3508

[9] T.R.F. Nonweiler, Aerodynamic problems of manned space vehicles, J. Royal Aeronaut. Soc. 63 (585) (1959) 521–528. https://doi.org/10.1017/S0368393100071662

[10] X. Zheng, Y. Li, C. Zhu, Y. You, Multiple osculating cones' waverider design method for ruled shock surfaces, AIAA J. 58 (2) (2020) 854–866. https://doi.org/10.2514/1.J058640

[11] F. Ding, J. Liu, C.-b. Shen, Z. Liu, S.-h. Chen, X. Fu, An overview of research on waverider design methodology, Acta Astronaut. 140 (2017) 190–205. https://doi.org/10.1016/j.actaastro.2017.08.027

[12] M.A. Zubin, N.A. Ostapenko, Experimental investigation of some singularities of the supersonic flow around V-shaped wings, Fluid Dyn. 10 (4) (1976) 647–652. https://doi.org/10.1007/BF01026712

[13] M.A. Zubin, N.A. Ostapenko, The flow structure near the windward side of V-shaped wings with an attached shock wave on the leading edges, Fluid Dyn. 21 (1) (1986) 104–112. https://doi.org/10.1007/BF01051109

[14] N.A. Ostapenko, Aerodynamic characteristics of V-shaped wings with shock waves detached from leading edges at hypersonic speeds, Fluid Dyn. 28 (4) (1993) 545–552. https://doi.org/10.1007/BF01342691

[15] I.I. Mazhul, R.D. Rakhcimov, Hypersonic power-law shaped waveriders in off-design regimes, J. Aircr. 41 (4) (2004) 839–845. https://doi.org/10.2514/1.386

[16] J.G. Jones, K.C. Moore, J. Pike, P.L. Roe, A method for designing lifting configurations for high supersonic speeds, using axisymmetric flow fields, Ingenieur-Archiv. 37 (1) (1968) 56–72. https://doi.org/10.1007/BF00532683

[17] K.G. Bowcutt, D. Capriotti, J.D. Anderson, Viscous optimised hypersonic waveriders, in: 25th AIAA Aerospace Sciences Meeting, American Institute of Aeronautics and Astronautics, Reston, Virigina, 1987. https://doi.org/10.2514/6.1987-272

[18] M. RASMUSSEN, Lifting-body configurations derived from supersonic flows past inclined circular and elliptic cones, in: 5th Atmospheric Flight Mechanics Conference for Future Space Systems, American Institute of Aeronautics and Astronautics, Reston, Virigina, 1979. https://doi.org/10.2514/6.1979-1665

[19] M.L. Rasmussen, Waverider configurations derived from inclined circular and elliptic cones, J. Spacecr. Rocket. 17 (6) (1980) 537–545. https://doi.org/10.2514/3.57771

[20] M.L. Rasmussen, M.C. Jischke, D.C. Daniel, Experimental forces and moments on cone-derived waveriders for M = 3 to 5, J. Spacecr. Rocket. 19 (6) (1982) 592–598. https://doi.org/10.2514/3.62306

[21] S.-C. Lin, Y.-S. Luo, Optimization of waverider configurations generated from inclined circular and elliptic cones, in: International Aerospace Planes and Hypersonics Technologies, American Institute of Aeronautics and Astronautics, Reston, Virigina, 1995. https://doi.org/10.2514/6.1995-6089

[22] K. Cui, G. Yang, The effect of conical flowfields on the performance of waveriders at Mach 6, Chin. Sci. Bull. 52 (1) (2007) 57–64. https://doi.org/10.1007/s11434-007-0026-2

[23] H. Sobieczky, F. Dougherty, K. Jones, Hypersonic waverider design from given shock waves, 1990.

[24] C. Liu, P. Bai, Waverider design using osculating method, AIAA J. 62 (5) (2024) 1643–1661. https://doi.org/10.2514/1.J063558

[25] P. Rodi, The osculating flowfield method of waverider geometry generation, in: 43rd AIAA Aerospace Sciences Meeting and Exhibit, American Institute of Aeronautics and Astronautics, Reston, Virigina, 2005. https://doi.org/10.2514/6.2005-511

[26] N. Takashima, M.J. Lewis, Wedge-cone waverider configuration for engine-airframe interaction, J. Aircr. 32 (5) (1995) 1142–1144. https://doi.org/10.2514/3.46848

[27] R.P. Starkey, M.J. Lewis, Simple analytical model for parametric studies of hypersonic waveriders, J. Spacecr. Rocket. 36 (4) (1999) 516–523.

[28] Z.-t. Zhao, W. Huang, L. Yan, Y.-g. Yang, An overview of research on wide-speed range waverider configuration, Prog. Aerosp. Sci. 113 (2020) 100606. https://doi.org/10.1016/j.paerosci.2020.100606

[29] J. Shi, L. Zhang, B. Jiang, B. Ai, Aerodynamic force and heating optimization of HTV-2 typed vehicle, in: 21st AIAA International Space Planes and Hypersonics Technologies Conference, 2017, p. 2374.

[30] K. Kontogiannis, A. Sóbester, N. Taylor, Efficient parameterization of waverider geometries, J. Aircr. 54 (3) (2017) 890–901. https://doi.org/10.2514/1.C033902

[31] J. Son, C. Son, K. Yee, A novel direct optimization framework for hypersonic waverider inverse design methods, Aerospace 9 (7) (2022) 348. https://doi.org/10.3390/aerospace9070348

[32] M.J. Lewis, Hypersonic missions and vehicle configurations, Encycloped. Aerosp. Eng. (2010).

[33] K.G. Bowcutt, Multidisciplinary optimization of airbreathing hypersonic vehicles, J. Propul. Power 17 (6) (2001) 1184–1190. https://doi.org/10.2514/2.5893

[34] R. Wuilbercq, Multi-disciplinary modelling of future space-access vehicles, Ph.D. thesis, University of Strathclyde, UK, 2015.

[35] N. Viola, P. Roncioni, O. Gori, R. Fusaro, Aerodynamic characterization of hypersonic transportation systems and its impact on mission analysis, Energies 14 (12) (2021) 3580. https://doi.org/10.3390/en14123580

[36] C. Bliamis, C. Menelaou, K. Yakinthos, Implementation of various-fidelity methods for viscous effects modeling on the design of a waverider, Aerosp. Sci. Technol. 133 (2023) 108141. https://doi.org/10.1016/j.ast.2023.108141

[37] A.S. Felix, Adjoint-Based Shape Optimisation of Hypersonic Vehicles, Master's thesis, Cranfield University, Cranfield, UK, 2023.

[38] M.F. Vizcaino, Aerodynamic shape optimisation of hypersonic waveriders using CFD and adjoint-based method, Master's thesis, Cranfield University, Cranfield, UK, 2023.

[39] J.R. Maxwell, Efficient design of viscous waveriders with CFD verification and off-design performance analysis, in: 53rd AIAA/SAE/ASEE Joint Propulsion Conference, American Institute of Aeronautics and Astronautics, Reston, Virginia, 2017. https://doi.org/10.2514/6.2017-4879

[40] F. Wang, H. Ding, M. Lei, Aerodynamic characteristics research on wide-speed range waverider configuration, Sci. China Ser. E: Technol. Sci. 52 (10) (2009) 2903–2910. https://doi.org/10.1007/s11431-009-0258-2

[41] S. Li, W. Huang, Z. Wang, J. Lei, Design and aerodynamic investigation of a parallel vehicle on a wide-speed range, Sci. China Inform. Sci. 57 (12) (2014) 1–10. https://doi.org/10.1007/s11432-014-5225-2

[42] J. Liu, Z. Liu, X. Wen, F. Ding, Novel osculating flowfield methodology for wide-speed range waverider vehicles across variable Mach number, Acta Astronaut. 162 (2019) 160–167. https://doi.org/10.1016/j.actaastro.2019.05.056

[43] P. Rodi, Vortex lift waverider configurations, in: 50th AIAA Aerospace Sciences Meeting Including the New Horizons Forum and Aerospace Exposition, American Institute of Aeronautics and Astronautics, Reston, Virigina, 2012. https://doi.org/10.2514/6.2012-1238

[44] F. Qu, T. Wang, C. Liu, J. Fu, J. Bai, Aerodynamic shape optimization of the vortex-shock integrated waverider over a wide speed range, Aerosp. Sci. Technol. 143 (2023) 108696. https://doi.org/10.1016/j.ast.2023.108696

[45] C. Liu, P. Bai, Y. Chen, B. Chen, Research on the design of double swept waverider, in: 21st AIAA International Space Planes and Hypersonics Technologies Conference, American Institute of Aeronautics and Astronautics, Reston, Virginia, 2017. https://doi.org/10.2514/6.2017-2140

[46] C. Tarpley, M.J. Lewis, Stability derivatives for a hypersonic caret-wing waverider, J. Aircr. 32 (4) (1995) 795–803. https://doi.org/10.2514/3.46793

[47] T. Bykerk, D. Verstraete, J. Steelant, Low speed longitudinal aerodynamic, static stability and performance analysis of a hypersonic waverider, Aerosp. Sci. Technol. 96 (2020) 105531. https://doi.org/10.1016/j.ast.2019.105531

[48] T. Bykerk, D. Verstraete, J. Steelant, Low speed lateral-directional aerodynamic and static stability analysis of a hypersonic waverider, Aerosp. Sci. Technol. 98 (2020) 105709. https://doi.org/10.1016/j.ast.2020.105709

[49] T. Bykerk, D. Verstraete, J. Steelant, Low speed longitudinal dynamic stability analysis of a hypersonic waverider using unsteady Reynolds averaged Navier Stokes forced oscillation simulations, Aerosp. Sci. Technol. 103 (2020) 105883. https://doi.org/10.1016/j.ast.2020.105883

[50] T. Bykerk, D. Verstraete, J. Steelant, Low speed lateral-directional dynamic stability analysis of a hypersonic waverider using unsteady Reynolds averaged Navier Stokes forced oscillation simulations, Aerosp. Sci. Technol. 106 (2020) 106228. https://doi.org/10.1016/j.ast.2020.106228

[51] W. Liu, C.-A. Zhang, X.-P. Wang, J.-J. Li, F.-M. Wang, Parametric study on lateral–directional stability of hypersonic waverider, AIAA J. (2021) 1–18. https://doi.org/10.2514/1.J059904

[52] J.D. Anderson, Jr, APPLIED HYPERSONIC AERODYNAMICS: HYPERSONIC WAVERIDERS, in: Fundamentals of Aerodynamics, McGraw-Hill Education, New York, 6 edition, 2016, pp. 908–921.

[53] J. Guo, G. Lin, X. Bu, L. Bai, Y. Chao, Parametric study on the heat transfer of a blunt body with counterflowing jets in hypersonic flows, Int. J. Heat Mass Transf. 121 (2018) 84–96. https://doi.org/10.1016/j.ijheatmasstransfer.2017.12.115

[54] W.A. Engblom, D.B. Goldstein, Nose-tip surface heat reduction mechanism, J. Thermophys Heat Transf. 10 (4) (1996) 598–606. https://doi.org/10.2514/3.835

[55] D. D'Orazio, DARPA's HTV-2 aircraft test flight failed due to heat stresses at Mach 20, 2012. https://www.theverge.com/2012/4/22/2967089/darpa-htv-2-results-mach-20.

[56] W.A. Engblom, D.B. Goldstein, D. Ladoon, S.P. Schneider, Fluid dynamics of hypersonic forward-facing cavity flow, J. Spacecr. Rocket. 34 (4) (1997) 437–444. https://doi.org/10.2514/2.3255

[57] P.E. Rodi, Integration of optimised leading edge geometries onto waverider configurations, in: 53rd AIAA Aerospace Sciences Meeting, 2015, p. 1700.

[58] W. Huang, L. Yan, J. Liu, L. Jin, J.-g. Tan, Drag and heat reduction mechanism in the combinational opposing jet and acoustic cavity concept for hypersonic vehicles, Aerosp. Sci. Technol. 42 (2015) 407–414. https://doi.org/10.1016/j.ast.2015.01.029

[59] W. Huang, Y.-p. Jiang, L. Yan, J. Liu, Heat flux reduction mechanism induced by a combinational opposing jet and cavity concept in supersonic flows, Acta Astronaut. 121 (2016) 164–171. https://doi.org/10.1016/j.actaastro.2016.01.008

[60] R. Kalimuthu, R.C. Mehta, E. Rathakrishnan, Drag reduction for spike attached to blunt-nosed body at Mach 6, J. Spacecr. Rocket. 47 (1) (2010) 219–222. https://doi.org/10.2514/1.46023

[61] W. Huang, L.-q. Li, L. Yan, T.-t. Zhang, Drag and heat flux reduction mechanism of blunted cone with aerodisks, Acta Astronaut. 138 (2017) 168–175. https://doi.org/10.1016/j.actaastro.2017.05.040

[62] X.-w. Sun, W. Huang, Z.-y. Guo, L. Yan, Multiobjective design optimization of hypersonic combinational novel cavity and opposing jet concept, J. Spacecr. Rocket. 54 (3) (2017) 662–671. https://doi.org/10.2514/1.A33801

[63] X. Chen, Z. Hou, H. Lietang, J. Liu, Multi-object optimization of waverider generated from conical flow and osculating cone, in: 46th AIAA Aerospace Sciences Meeting and Exhibit, American Institute of Aeronautics and Astronautics, Reston, Virigina, 2008. https://doi.org/10.2514/6.2008-131

[64] D. Stevens, Practical considerations in waverider applications, in: Guidance, Navigation and Control Conference, American Institute of Aeronautics and Astronautics, Reston, Virigina, 1992. https://doi.org/10.2514/6.1992-4247

[65] T. Eggers, H. Sobieczky, K. Center, Design of advanced waveriders with high aerodynamic efficiency, in: 5th International Aerospace Planes and Hypersonics Technologies Conference, American Institute of Aeronautics and Astronautics, Reston, Virigina, 1993. https://doi.org/10.2514/6.1993-5141

[66] S.Q. Guo, W. Liu, C.A. Zhang, Y. Liu, F.M. Wang, Aerodynamic optimization of hypersonic blunted waveriders based on symbolic regression, Aerosp. Sci. Technol. 144 (2024) 108801.

[67] D.J. Poole, C.B. Allen, T.C.S. Rendall, Metric-based mathematical derivation of efficient airfoil design variables, AIAA J. 53 (5) (2015) 1349–1361. https://doi.org/10.2514/1.J053427

[68] A. Jameson, Aerodynamic design via control theory, J. Sci. Comput. 3 (3) (1988) 233–260. https://doi.org/10.1007/BF01061285

[69] C. Rovira Sala, M. Famada Vizcaino, A. Felix Simon, A. Bernabeu-Vasquez, B. Van Hove, T.I. Józsa, J.-J. O.E. Hoste, An exploration of adjoint-based optimization for hypersonic vehicle- and propulsion design, HiSST, Busan, 2024.

[70] C. Rovira Sala, N. Jalaei Poustian, J.-J. O.E. Hoste, T.I. Józsa, Computational fluid dynamics and adjoint-based optimization of a supersonic combustor for improved efficiency, Fluids 10 (11) (2025). https://doi.org/10.3390/fluids10110284

[71] F. Qu, T. Wang, C. Liu, J. Fu, J. Bai, Aerodynamic shape optimization of the vortex-shock integrated waverider over a wide speed range, Aerosp. Sci. Technol. 143 (2023) 108696.

[72] N. Morita, T. Tsuchiya, H. Taguchi, MDO of hypersonic waverider with trajectory-aero-structure coupling, in: 23rd AIAA International Space Planes and Hypersonic Systems and Technologies Conference, American Institute of Aeronautics and Astronautics, Reston, Virginia, 2020. https://doi.org/10.2514/6.2020-2402

[73] D.J. Poole, C.B. Allen, T. Rendall, Comparison of local and global constrained aerodynamic shape optimization, in: 32nd AIAA Applied Aerodynamics Conference, American Institute of Aeronautics and Astronautics, Reston, Virginia, 2014. https://doi.org/10.2514/6.2014-3223

[74] W. Liu, C.-A. Zhang, F.-M. Wang, Z.-Y. Ye, Design and optimization method for hypersonic quasi-Waverider, AIAA J. 58 (5) (2020) 2132–2146. https://doi.org/10.2514/1.J059087
[75] P.E. Rodi, Waverider vehicle optimization with volumetric constraints for sonic boom, in: 2018 AIAA Aerospace Sciences Meeting, American Institute of Aeronautics and Astronautics, Reston, Virginia, 2018. https://doi.org/10.2514/6.2018-0551
[76] A. Ghosh, S. Rao, Development of maximum conical shock angle limit for osculating cone waveriders, Aerosp. Sci. Technol. 147 (2024) 109031.
[77] Siemens Digital Industries Software, Simcenter STAR-CCM+ 2402 (19.02.009-R8), 2024.
[78] J. Nassif, Waverider Generator 2.0.1, 2024, https://github.com/jade5638/waverider_generator.
[79] J. Nassif, Multi-Objective Multi-Point Optimization of a Hypersonic waverider, Master's thesis, Cranfield University, Cranfield, UK, 2024.
[80] K. Kontogiannis, On developing efficient parametric geometry models for waverider-based hypersonic aircraft, Ph.D. thesis, University of Southampton, 2017.
[81] D. Cowden, J. Cook, cadquery 2.4.0, 2024. https://pypi.org/project/cadquery/.
[82] K.G. Bowcutt, J.D. Anderson, D. Capriotti, Numerical optimization of conical flow waveriders including detailed viscous effects, Aerodyn. Hyperson. Lifting Vehicl. (1987).
[83] P.G. Cross, M.R. West, Simulation of Hypersonic Flowfields Using Star-CCM+, China Lake, CA, USA: Naval Air Warfare Center Weapons Division (2019).
[84] M.-S. Liou, A Sequel to AUSM: AUSM+, J. Comput. Phys. 129 (2) (1996) 364–382. https://doi.org/10.1006/jcph.1996.0256
[85] J.A. Meijerink, H.A. van der Vorst, An iterative solution method for linear systems of which the coefficient matrix is a symmetric M-matrix, Math. Comput. 31 (137) (1977) 148. https://doi.org/10.2307/2005786
[86] V. Venkatakrishnan, On the accuracy of limiters and convergence to steady state solutions, in: 31st Aerospace Sciences Meeting, American Institute of Aeronautics and Astronautics, Reston, Virigina, 1993. https://doi.org/10.2514/6.1993-880
[87] D.G. Fletcher, Fundamentals of Hypersonic Flow-Aerothermodynamics, Critical Technologies for Hypersonic Vehicle Development (Von Karman Inst. for Fluid Dynamics, Rhode-St-Genese, 2005) (2004) 1–3.
[88] R.N. Gupta, K.-P. Lee, R.A. Thompson, J.M. Yos, Calculations and curve fits of thermodynamic and transport properties for equilibrium air to 30000 K, Technical Report, 1991.
[89] P. Saves, R. Lafage, N. Bartoli, Y. Diouane, J. Bussemaker, T. Lefebvre, J.T. Hwang, J. Morlier, J.R.R.A. Martins, SMT 2.0: A surrogate modeling toolbox with a focus on hierarchical and mixed variables gaussian processes, Adv. Eng. Softw. 188 (2024) 103571. https://doi.org/https://doi.org/10.1016/j.advengsoft.2023.103571
[90] M.D. McKay, R.J. Beckman, W.J. Conover, A comparison of three methods for selecting values of input variables in the analysis of output from a computer code, Technometrics 21 (2) (1979) 239. https://doi.org/10.2307/1268522
[91] F. Pedregosa, G. Varoquaux, A. Gramfort, V. Michel, B. Thirion, O. Grisel, M. Blondel, P. Prettenhofer, R. Weiss, V. Dubourg, J. Vanderplas, A. Passos, D. Cournapeau, M. Brucher, M. Perrot, E. Duchesnay, Scikit-learn: machine learning in Python, J. Mach. Learn. Res. 12 (85) (2011) 2825–2830. http://jmlr.org/papers/v12/pedregosa11a.html.
[92] J.H. Holland, Adaptation in Natural and Artificial Systems: an Introductory Analysis with Applications to Biology, Control, and Artificial Intelligence, MIT press, 1992.
[93] A.F. Gad, Pygad: an intuitive genetic algorithm python library, Multimed. Tool. Appl. (2023) 1–14. https://doi.org/https://doi.org/10.48550/arXiv.2106.06158
[94] L. Breiman, Random forests, Mach. Learn. 45 (1) (2001) 5–32. https://doi.org/10.1023/A:1010933404324
[95] F. Ding, J. Liu, C.-b. Shen, W. Huang, Novel approach for design of a waverider vehicle generated from axisymmetric supersonic flows past a pointed von Karman ogive, Aerosp. Sci. Technol. 42 (2015) 297–308.

DSPACE

https://dspace.org/

Multi-point surrogate-based aerodynamic optimisation of a generic hypersonic waverider

Nassif, Jade; Hoste, Jimmy-John OE; Józsa, Tamás I.

2026-08
Elsevier
https://doi.org/10.1016/j.ast.2026.111978
Nassif J, Hoste J-JOE, Józsa TI. (2026) Multi-point surrogate-based aerodynamic optimisation of a generic hypersonic waverider. Aerospace Science and Technology, Volume 175, August 2026, Article number 111978

Downloaded from a DSpace repository. https://dspace.org/